Ternary molybdate $Rb_5(Ag_{1/3}Hf_{5/3})(MoO_4)_6$: synthesis, structure, thermal expansion and ionic conductivity

Alexey Subanakov [ab] * [iD], Yunna Tushinova [ab] [iD], Evgeny Kovtunets [a] [iD],
Tatyana Spiridonova [a] [iD], Bair Bazarov [ab] [iD]

a: Laboratory of oxide systems, Baikal Institute of Nature Management SB RAS, Ulan-Ude, 670047, Russia
b: Institute of Natural Sciences, The Banzarov State University of Buryatia, Ulan-Ude, 670000, Russia
* Corresponding author: subanakov@binm.bscnet.ru

Abstract

This study aims to characterize the properties of the ternary molybdate $Rb_5(Ag_{1/3}Hf_{5/3})(MoO_4)_6$, which was previously identified during phase equilibrium investigations in the Ag_2MoO_4–Rb_2MoO_4–$Hf(MoO_4)_2$ system. A ternary molybdate $Rb_5(Ag_{1/3}Hf_{5/3})(MoO_4)_6$ was obtained through a solid-state reaction. It was found that the compound crystallizes in the trigonal space group $R\bar{3}c$ and melts at 596 °C with decomposition. Its structure was refined using the Rietveld method. The crystal structure consists of a mixed framework composed of isolated $(Ag/Hf)O_6$ octahedra and MoO_4 tetrahedra, interconnected through shared oxygen vertices. Large voids within the framework accommodate two types of rubidium atoms. Using the powder XRD data recorded over 30–400 °C, the principal components of the thermal expansion tensor were determined. $Rb_5(Ag_{1/3}Hf_{5/3})(MoO_4)_6$ can be classified as a material with high thermal expansion coefficient (α_V = 36.7·10^{-6} °C^{-1} at 400 °C). At elevated temperatures, the compound exhibited significant ionic conductivity, reaching 1.7·10^{-3} S/cm at 480 °C with an activation energy E_a = 0.8 eV with oxygen ions as the probable charge carriers. Energy barriers for one-, two-, and three-dimensional transport in the compound were theoretically evaluated using the softBV program and bond valence sum maps (BVS).

Key findings

● $Rb_5(Ag_{1/3}Hf_{5/3})(MoO_4)_6$ was successfully synthesized, and its structural properties were characterized using powder X-ray diffraction techniques.

● The compound can be classified as a material with high thermal expansion.

● The compound exhibited high ionic conductivity of 1.7·10^{-3} S/cm at 480 °C.

1. Introduction

The search for new functional materials remains an important task of modern materials science. Compounds based on double and triple molybdates are promising for the preparation of functional materials. Molybdates, encompassing a vast array of compounds with diverse compositions and structures, have emerged as a significant class of functional materials due to their remarkable and tunable physicochemical properties. Their versatility stems from the ability to incorporate various metal cations into the molybdate framework, leading to a wide range of functionalities. For example, high oxygen conductivity was reported for molybdates with fluorite [1–8],

perovskite [9–14], and $La_2Mo_2O_9$ [15–18] structures. Furthermore, some oxygen-conducting complex molybdenum oxides also exhibit proton conductivity [4, 8, 19], broadening their potential applications. Current research focuses extensively on complex molybdates with diverse compositions to identify materials exhibiting desirable physicochemical properties, including high ionic conductivity [20–25], negative thermal expansion [26–28], catalytic activity [29, 30], luminescence [31], and microwave dielectric properties [31]. The development of numerous new functional materials relies on ongoing research into the physicochemical properties of new compounds. The synthesis and characterization of new compounds contribute significantly to our understanding of fundamental

chemical and physical principles, which is necessary for functional materials creation.

The study of ternary molybdate systems Rb_2MoO_4–$AMoO_4$–$R(MoO_4)_2$, (where A represents divalent metals and R represents Zr or Hf), yielded new triple molybdates $Rb_5A_{0.5}R_{1.5}(MoO_4)_6$. Moreover, they crystallize in two structural types: $R3c$ [32] with an ionic radii of a divalent metal less than 1 Å (Ni, Mg, Cu, Zn, Co, Mn, Cd) and $R\overline{3}$ [33] (Ca, Sr, Ba, Pb). Further investigation is needed to fully elucidate their crystal structures and cation ordering. In addition, the compound's properties are significantly influenced by the distribution of atoms within the crystal lattice.

The object of this study is a triple molybdate $Rb_5(Ag_{1/3}Hf_{5/3})(MoO_4)_6$ which were reported for the first time in the study of the Ag_2MoO_4–Rb_2MoO_4–$Hf(MoO_4)_2$ system [34]. In [34], the authors determined the unit cell parameters using Le Bail fitting and the melting point using differential scanning calorimetry.

The goal of this work is to study the triple molybdate $Rb_5(Ag_{1/3}Hf_{5/3})(MoO_4)_6$ in terms of the crystal structure based on Rietveld refinement with the attention to atoms distribution within the crystal lattice, thermal behavior, and ionic conductivity.

2. Experimental

Commercially available reagents were used as starting materials for the synthesis: Rb_2CO_3 (high purity), HfO_2 (chemically pure), $AgNO_3$ (analytical grade), and MoO_3 (analytical grade). The ternary molybdate $Rb_5(Ag_{1/3}Hf_{5/3})(MoO_4)_6$ was synthesized from a stoichiometric mixture of Ag_2MoO_4, Rb_2MoO_4, and $Hf(MoO_4)_2$. These molybdates were obtained by solid state reactions from stoichiometric mixtures of the respective reagents. Stepwise annealing of the samples was performed in a muffle furnace. During annealing, the samples were repeatedly ground with the addition of ethyl alcohol. Silver molybdate was synthesized at temperatures of 200–450 °C for 150 h. Rubidium molybdate was synthesized at 400–550 °C, while hafnium molybdate was synthesized at 400–750 °C, with both processes lasting 80–100 h.

X-ray diffraction analysis (XRD) was performed using a Bruker D8 Advance automated powder diffractometer (VANTEC detector, Cu Kα radiation, λ = 1.5418 Å, Bragg-Brentano geometry). XRD data were collected at 296 K in the range 2θ = 7–100° in steps of 0.02076°. The ICDD PDF-2 database was used for diffractogram analysis.

Rietveld refinement was conducted using the TOPAS 4.2 software [35, 36].

The surface morphology and analysis of chemical composition were examined by SEM microscopy at room temperature using a Hitachi SEM TM-1000 with detector TM-1000 TDS.

High-temperature powder X-ray diffraction (HT-PXRD) was also employed to characterize the ternary molybdate. Measurements were conducted using the abovementioned diffractometer with an Anton Paar HTK16 high-temperature chamber over a temperature range of 30–500 °C in steps of 50 °C. Finely ground sample was applied to a platinum sample holder using a hexane suspension. An external Si standard was used to control the 2θ correction prior to the measurements. Lattice parameters were calculated using the Topas 4.2 software package, while visualization and calculation of the thermal expansion tensor were conducted with the TTT software package [37]. The temperature dependence of the lattice parameters was approximated using a straight line. Based on the obtained data, the principal values of the thermal expansion tensor were calculated, and cross sections of the thermal expansion coefficient were plotted.

Theoretical estimation of the activation energy and ion transport pathways in the ternary molybdate was performed using the softBV program [38] with bond valence sum maps (BVS).

An STA 449 F1 Jupiter thermal analyser (NETZSCH) was used for thermogravimetric (TG) and differential scanning calorimetric (DSC) characterization of the title compound. The thermal analysis was carried out in the temperature range of 25–650 °C in argon flow at a rate of 10 °C/min, using platinum crucible. The use of Pt–PtRh thermocouple increased the accuracy of temperature measurement to ±1°.

Electrical conductivity measurements were conducted over a temperature range of 200–480 °C using a Z-1500J impedance meter in both heating and cooling modes (2 °C/min) across a frequency range of 1 Hz–1 MHz. To investigate the ion-conducting properties of $Rb_5(Ag_{1/3}Hf_{5/3})(MoO_4)_6$, its ceramic samples in the form of disk-shaped pellets (d = 10 mm, h = 1.7 mm) were prepared by pressing the powder at 1 kbar and sintering at 500 °C for 4 h. Electrodes were applied to the pellets surfaces by firing colloidal platinum for 1 h.

3. Results and Discussion

3.1. Synthesis of $Rb_5(Ag_{1/3}Hf_{5/3})(MoO_4)_6$

The sequences of chemical transformations occurring during the formation of $Rb_5(Ag_{1/3}Hf_{5/3})(MoO_4)_6$ were established. Three-component stoichiometric mixture of Ag_2MoO_4, Rb_2MoO_4, and $Hf(MoO_4)_2$ was annealed over a temperature range of 290–500 °C in increments of 30 °C. X-ray diffraction patterns obtained at intermediate stages of calcination, showing the transformations of phases, are given in the Figure S1. The reaction sequence, as determined by powder XRD analysis, is illustrated in the following scheme:
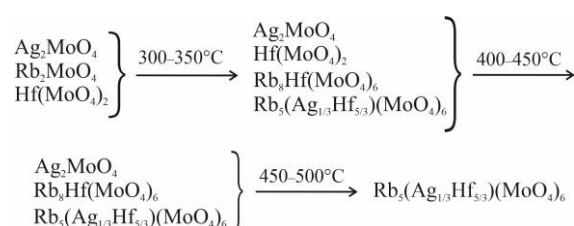
Based on these results, the pure triple molybdate was synthesized by annealing at 450-500 °C for 60 h.

SEM micrograph of the synthesized powder shows aggregation of particles up to 20 μm in size with a flaky surface (Figure S2).

3.2. Rietveld refinement and structure of Rb$_5$(Ag$_{1/3}$Hf$_{5/3}$)(MoO$_4$)$_6$

All XRD peaks of Rb$_5$(Ag$_{1/3}$Hf$_{5/3}$)(MoO$_4$)$_6$ could be indexed in a trigonal unit cell (space group $R\bar{3}c$), with initial lattice parameters and atomic positions closely matching those of Rb$_5$Co$_{0.5}$Hf$_{1.5}$(MoO$_4$)$_6$ [39], which served as the starting model for Rietveld refinement. Silver and hafnium ions were positioned in two crystallographic sites, Co1/Hf1 and Co2/Hf2, and their occupancies were refined. A Pearson VII function was used to describe peak shapes. Refinement was performed by gradually introducing parameters with simultaneous graphical modeling of the background. To reduce the number of refined parameters, isotropic displacement parameters (B_{iso}) for the O atoms were assumed to be equivalent.

The refinement was stable with low residual R-factors. The refinement results for Rb$_5$(Ag$_{1/3}$Hf$_{5/3}$)(MoO$_4$)$_6$ are presented in Table 1, key interatomic distances in Table S1, and atomic coordinates and isotropic displacement parameters in Table S2, while the calculated and experimental XRD patterns with the difference curve are shown in Figure 1.

The crystallographic data for Rb$_5$(Ag$_{1/3}$Hf$_{5/3}$)(MoO$_4$)$_6$ were deposited at the Cambridge Crystallographic Data Centre (deposition number CSD 2388190) and are available on the website www.ccdc.cam.ac.uk/data_request/cif.

The crystal structure consists of a mixed framework composed of isolated (Ag/Hf)O$_6$ octahedra and MoO$_4$ tetrahedra, interconnected through shared oxygen vertices. Large voids within the framework accommodate two types of rubidium atoms (Figure 2). The Rb1 atom exhibits a nine-coordinate oxygen environment, with Rb–O bond distances spanning from 2.84(1) to 3.25(1) Å. The second rubidium atom (Rb2) is coordinated to 12 oxygen atoms, forming a cuboctahedral environment. The Rb–O bond lengths in this coordination vary from 2.99(1) to 3.52(1) Å.

Table 1 Main parameters of processing and refinement of the Rb$_5$(Ag$_{1/3}$Hf$_{5/3}$)(MoO$_4$)$_6$ sample.

Compound	Rb$_5$(Ag$_{1/3}$Hf$_{5/3}$)(MoO$_4$)$_6$
Sp.Gr.	trigonal, $R\bar{3}c$
a, Å	10.70994 (6)
c, Å	38.5395 (5)
V, Å^3	3828.35 (7)
Z	6
2θ-interval, º	8–100
R_{wp}, %	4.77
R_p, %	3.78
R_{exp}, %	2.15
χ^2	2.22
R_B, %	2.24

Both (Ag/Hf)O$_6$ octahedra are primarily occupied by hafnium with a minor silver content. (Ag1/Hf1)O$_6$ exhibits an Ag/Hf ratio of 0.21(1)/0.79(1) and an Ag/Hf–O distance of 2.12(1) Å. In contrast, (Ag2/Hf2)O$_6$ has approximately half the silver content, with an Ag/Hf ratio of 0.123(12)/0.877(12) and an Ag/Hf–O distance of 2.20(1) Å. The site occupancies can be compared to those reported for the similar triple molybdates Rb$_5$Co$_{0.5}$Hf$_{1.5}$(MoO$_4$)$_6$ [39] and K$_5$ScHf(MoO$_4$)$_6$ [40]. The distribution of Co^{2+} equals M1 – Hf0.85(1)/Co0.15(1), M2 – Hf0.66(2)/Co0.34(2) in Rb$_5$Co$_{0.5}$Hf$_{1.5}$(MoO$_4$)$_6$ [39] and Sc^{3+} – M1 – Hf0.548(4)/Sc0.452(4), M2 – Hf0.452(4)/Sc0.548(4) in K$_5$ScHf(MoO$_4$)$_6$ [40]. As seen, a general trend emerges: as cation charge increases, so does its overall concentration. In addition, Co^{2+} ions show a stronger preference for the Hf2 site (Wyckoff position 6a, point group 32) compared to Ag$^+$. Sc^{3+} ions display a more uniform distribution across both sites; however, the larger cation still exhibits a slight preference for the Hf2 site, with approximately 20% higher occupancy compared to the Hf1 site.

3.3. Thermal behavior

Thermal behavior of Rb$_5$(Ag$_{1/3}$Hf$_{5/3}$)(MoO$_4$)$_6$ *in situ* was investigated using simultaneous thermal analysis (DSC and TG) (Figure 3) and high-temperature powder X-ray diffraction (HT-PXRD). Simultaneous thermal analysis (DSC and TG) was used to study Rb$_5$(Ag$_{1/3}$Hf$_{5/3}$)(MoO$_4$)$_6$ over a temperature range from room temperature to 650 °C. No mass change was recorded throughout the temperature range. Incongruent melting of the compound was observed at 596 °C that is in agreement with [34]. X-ray diffraction (XRD) analysis of the residue after melting of the title compound revealed Rb$_8$Hf(MoO$_4$)$_6$ as the dominant phase.

The unit cell parameters of Rb$_5$(Ag$_{1/3}$Hf$_{5/3}$)(MoO$_4$)$_6$ were determined using high-temperature powder X-ray diffraction (HT-PXRD) between 30 and 400 °C. Figure 4 and Table S3 present the temperature-dependent behavior of the a, c, and V parameters, all of which exhibit a linear increase with temperature. The coefficients of thermal expansion (CTE) were calculated from these data using linear fits (Table S4) and are summarized in Table S5.
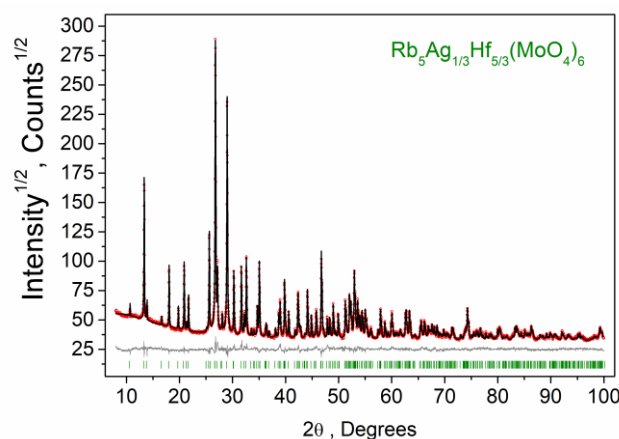

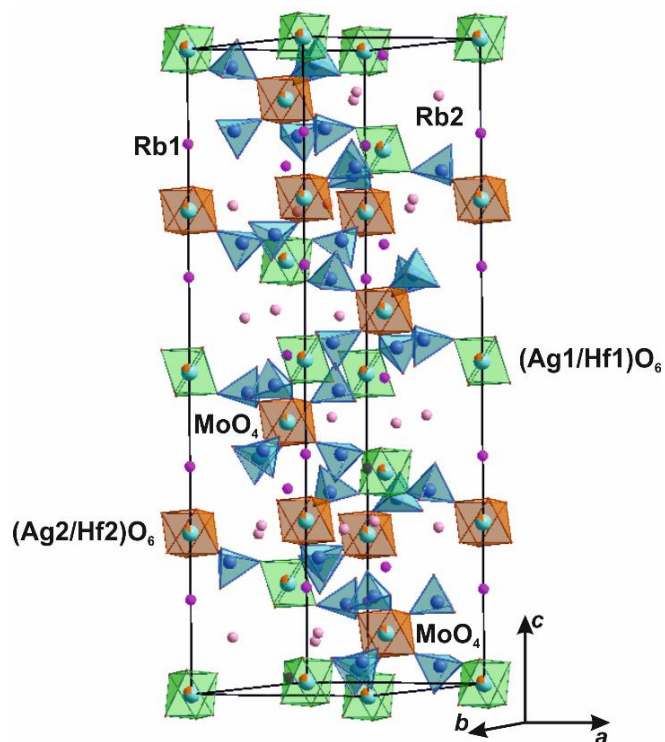**Figure 1** Difference Rietveld plot of Rb$_5$(Ag$_{1/3}$Hf$_{5/3}$)(MoO$_4$)$_6$.

Figure 2 Crystal structure of $Rb_5(Ag_{1/3}Hf_{5/3})(MoO_4)_6$.

Figure 3 DSC and TG heating curve of $Rb_5(Ag_{1/3}Hf_{5/3})(MoO_4)_6$.

Figure 5 compares the cross-section of the thermal expansion tensor with the projection of the crystal structure onto the ac plane.

The CTE values, α_a and α_c, remain relatively constant throughout the investigated temperature range, with values of $11.2 \cdot 10^{-6}$ °C^{-1} and $14.3 \cdot 10^{-6}$ °C^{-1}, respectively (Table S5).

At 400 °C, the volumetric thermal expansion coefficient (α_V) of $Rb_5(Ag_{1/3}Hf_{5/3})(MoO_4)_6$ is $36.7 \cdot 10^{-6}$ °C^{-1}. Based on its α_V value, $Rb_5(Ag_{1/3}Hf_{5/3})(MoO_4)_6$ can be classified as a material with high thermal expansion [41]. The α_V of $Rb_5(Ag_{1/3}Hf_{5/3})(MoO_4)_6$ is comparable to that of $K_5Mn_{0.5}Zr_{1.5}(MoO_4)_6$ [42] but approximately 30% lower than $K_5Pb_{0.5}Zr_{1.5}(MoO_4)_6$ [43]. $Rb_5(Ag_{1/3}Hf_{5/3})(MoO_4)_6$ demonstrates a weak anisotropy with an $\alpha_{max}/\alpha_{min}$ ratio of approximately 1.3 across the entire temperature range (Table S5). Among the studied similar structure analogs, $Rb_5(Ag_{1/3}Hf_{5/3})(MoO_4)_6$ exhibits the lowest degree of thermal expansion anisotropy (Table 2).

Table 2 Unit cell parameters and CTLR for $Rb_5(Ag_{1/3}Hf_{5/3})(MoO_4)_6$ and closely related structural analogues.

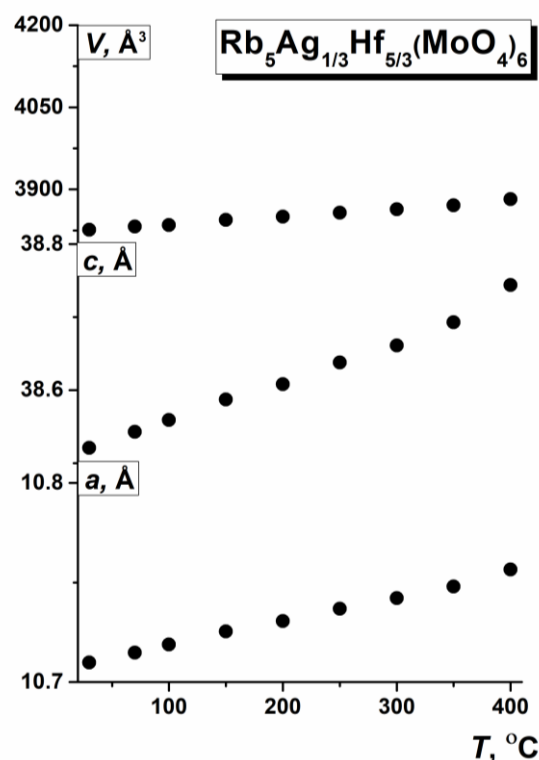|	$Rb_5(Ag_{1/3}Hf_{5/3})$ $(MoO_4)_6$ (this work)	$K_5Mn_{0.5}Zr_{1.5}$ $(MoO_4)_6$ [41]	$K_5Pb_{0.5}Zr_{1.5}$ $(MoO_4)_6$ [42]
trigonal	$R\bar{3}c$	$R3c$	$R\bar{3}$
a, Å	10.70994 (6)	10.6026(1)	10.6604 (2)
c, Å	38.5395 (5)	37.6253(5)	37.9769 (9)
V, Å^3	3828.35 (7)	3663.0(1)	3737.6 (2)
α_a [a]	11.3(2)	10.9(2)	11.3(1)
α_c [a]	14.7(6)	20(1)	33(1)
α_V [a]	37.3(1)	41.7(1)	55.7(1)
$\alpha_{max}/\alpha_{min}$	1.3	1.8	2.9

[a] $\cdot 10^{-6}$ °C^{-1} at 400 °C

Figure 4 The temperature dependences of the unit cell parameters of $Rb_5(Ag_{1/3}Hf_{5/3})(MoO_4)_6$.

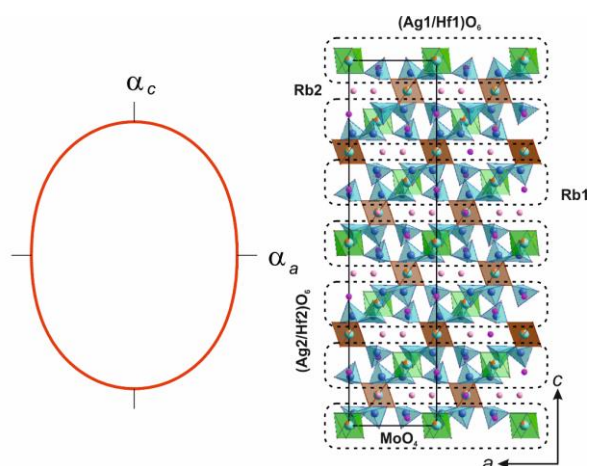**Figure 5** Projection of the crystal structure of $Rb_5(Ag_{1/3}Hf_{5/3})(MoO_4)_6$ on the bc plane in comparison with the cross sections of the thermal expansion tensor. The "quasi" 2D (two-dimensional) layers are highlighted by dotted lines.

The thermal expansion behavior of $Rb_5(Ag_{1/3}Hf_{5/3})(MoO_4)_6$ can be understood within the framework of the "rigid unit mode" (RUM) concept, which was applied to framework materials [44]. This model considers the interaction between rigid HfO_6 octahedra, MoO_4 tetrahedra, and relatively flexible AgO_6 octahedra (Figure 5). The thermal expansion in the *ab* plane is primarily driven by the deformation of Ag1–O bonds as temperature increases. The weak anisotropy and expansion along the *c* direction can be attributed to the presence of fewer deformable Ag2–O bonds in the interlayer space and the complete absence of "hard" Mo–O bonds in this region.

3.4. Electrical conductivity

Impedance plots for $Rb_5(Ag_{1/3}Hf_{5/3})(MoO_4)_6$ were constructed based on the measurement data, (Figure 6). At low temperatures, these plots displayed a semicircle shape (e.g., Figure 6, 200 °C) starting from the origin, while at higher temperatures (e.g., Figure 6, 300 °C), they showed a semicircle combined with a low-frequency tail. The tail in the graph corresponds to electrode processes.

Figure 7 presents the temperature dependence of conductivity for $Rb_5(Ag_{1/3}Hf_{5/3})(MoO_4)_6$. The conductivity varied non-monotonically with temperature, showing two distinct segments on both the heating and cooling curves. During heating from 200 °C to 360 °C, the conductivity increased linearly from $8.9 \cdot 10^{-7}$ S/cm to $6.1 \cdot 10^{-5}$ S/cm (with activation energy E_a = 0.9 eV). Upon further heating to 480 °C, the conductivity sharply raised to $1.7 \cdot 10^{-3}$ S/cm (E_a = 0.8 eV). On the cooling curve, the temperature segments shifted: in the first segment, observed from 480 to 330 °C, conductivity decreased from σ = $1.7 \cdot 10^{-3}$ to $1.2 \cdot 10^{-4}$ S/cm (E_a = 0.8 eV). In the second segment, from 320 to 200°C, conductivity further decreased from σ = $5.2 \cdot 10^{-5}$ to $8.4 \cdot 10^{-7}$ S/cm (E_a = 1.0 eV). This thermal hysteresis was characteristic of a diffuse first-order phase transition in the compound.

The conductivity and activation energy values for $Rb_5(Ag_{1/3}Hf_{5/3})(MoO_4)_6$ at 480 °C are comparable to those of the similar trigonal triple molybdates (Table 3).

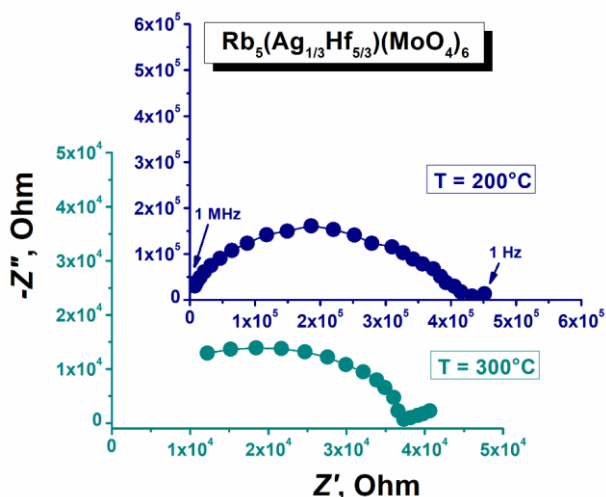**Figure 6** The impedance plots of $Rb_5(Ag_{1/3}Hf_{5/3})(MoO_4)_6$.

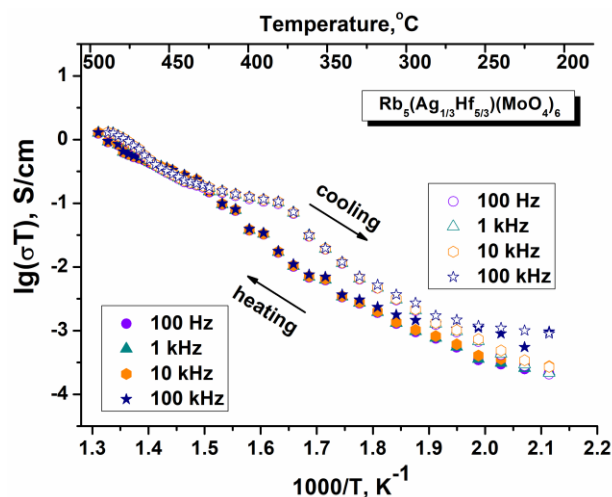**Figure 7** The temperature dependence of the conductivity of $Rb_5(Ag_{1/3}Hf_{5/3})(MoO_4)_6$.

Table 3 Conductivity characteristics of ternary molybdates $Rb_5(M_{1/3}R_{5/3})(MoO_4)_6$.

Compound	Conductivity σ, S/cm (480°C)	Activation energy E_a, eV
$Rb_5(Na_{1/3}Zr_{5/3})(MoO_4)_6$ [45]	$3.1 \cdot 10^{-3}$	0.6–0.8
$Rb_5(Ag_{1/3}Zr_{5/3})(MoO_4)_6$ [45]	$1.8 \cdot 10^{-3}$	0.6–0.8
$Rb_5(Ag_{1/3}Hf_{5/3})(MoO_4)_6$ (this work)	$1.7 \cdot 10^{-3}$	0.8

A theoretical evaluation of the energy barriers for one-, two-, and three-dimensional ion transport in $Rb_5(Ag_{1/3}Hf_{5/3})(MoO_4)_6$ using the softBV program and bond valence sum maps (BVS) was conducted. Silver, rubidium, and oxygen ions were considered as the most likely mobile ions. The analysis of the calculations indicated that in this structure, two-dimensional oxygen ion diffusion with an energy barrier of 0.713 eV occurs along the (001) plane, while three-dimensional oxygen transport with E_b = 0.718 eV is also possible (Figure 8). The movement of rubidium and silver ions is less likely due to their high energy barriers (Table S6). Iso-surfaces encompass (Hf, Ag)O_6 octahedra and MoO_4 tetrahedra, which are connected through shared oxygen vertices (Figure S4). Experimental verification of the theoretical calculations results of oxygen conductivity will be the subject of future works.
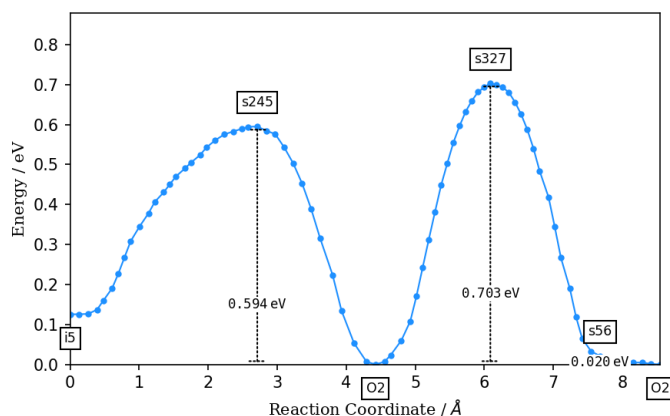

Figure 8 Energy profile of oxygen transport in the structure of $Rb_5(Ag_{1/3}Hf_{5/3})(MoO_4)_6$.

4. Limitation

To gain better interpretation of electrical conductivity, the experimental verification of the theoretical calculations results of oxygen conductivity will be done in the future.

5. Conclusions

This work extends our insight into the physicochemical properties of triple molybdates containing mono- and tetravalent metals. $Rb_5(Ag_{1/3}Hf_{5/3})(MoO_4)_6$ was synthesized via the solid-state reaction, and its crystal structure was refined using the Rietveld method, employing initial parameters based on $Rb_5Co_{0.5}Hf_{1.5}(MoO_4)_6$. The compound crystallizes in the sp. gr. $R\overline{3}c$ and belongs to a rather large group of trigonal compounds with a ~9–10 Å and long c parameters [46, 47]. These triple molybdates are characterized by the framework structures built from isolated MO_6 octahedra and MoO_4 tetrahedra, with distinctive arrangements of polyhedra that create cavities of various shapes and allow diverse isomorphic substitutions.

This study revealed significant ionic conductivity in $Rb_5(Ag_{1/3}Hf_{5/3})(MoO_4)_6$, reaching a value of $1.7 \cdot 10^{-3}$ S/cm at 480 °C with an activation energy of 0.8 eV. High-temperature powder X-ray diffraction was used to investigate the thermal expansion of $Rb_5(Ag_{1/3}Hf_{5/3})(MoO_4)_6$. The title compound can be classified as a high-expansion material with low anisotropy. Further investigation of thermophysical properties within this structural type is required to elucidate the influence nature of elements on thermal expansion coefficients and anisotropy.

Supplementary materials

This manuscript contains supplementary materials, which are available on the corresponding online page.

Table S1: Fractional atomic coordinates and isotropic displacement parameters (Å²) of $Rb_5(Ag_{1/3}Hf_{5/3})(MoO_4)_{66}$.

Table S2: Main bond lengths (Å) of $Rb_5(Ag_{1/3}Hf_{5/3})(MoO_4)_6$.

Table S3: The unit cell parameters of $Rb_5(Ag_{1/3}Hf_{5/3})(MoO_4)_6$ over the temperature range 30–400 °C.

Table S4: Temperature dependencies of the unit-cell parameters approximated by linear polynomial functions $a_0+a_1 \cdot 10^{-3}t^2$ in the temperature range 30–400 °C.

Table S5: Thermal expansion coefficients ($\times 10^{-6}$°C^{-1}) of $Rb_5(Ag_{1/3}Hf_{5/3})(MoO_4)_6$.

Table S6: Calculated migration maps and energy barrier values of testing ions in $Rb_5(Ag_{1/3}Hf_{5/3})(MoO_4)_6$.

Figure S1 Rietveld plot of $Rb_5(Ag_{1/3}Hf_{5/3})(MoO_4)_6$ at 350 °C and 450 °C.

Figure S2 SEM microphotographs of the $Rb_5(Ag_{1/3}Hf_{5/3})(MoO_4)_6$ synthesized powder.

Figure S3 The chemical composition of the $Rb_5(Ag_{1/3}Hf_{5/3})(MoO_4)_6$. Aluminum contamination was detected from the substrate.

Figure S4: Calculated iso-surfaces of activation energies for oxygen ion transport (red) in the structure of $Rb_5(Ag_{1/3}Hf_{5/3})(MoO_4)_6$.

Acknowledgments

Author contributions

Conceptualization: A.K.S., Yu.L.T., E.V.K., T.S.S., B.G.B.
Formal Analysis: E.V.K., T.S.S.
Investigation: Yu.L.T., E.V.K., T.S.S.
Methodology: A.K.S., Yu.L.T., E.V.K., T.S.S., B.G.B.
Software: E.V.K., T.S.S.
Supervision: A.K.S., B.G.B.
Visualization: A.K.S., E.V.K., T.S.S.
Writing – original draft: A.K.S., Yu.L.T., E.V.K., T.S.S.
Writing – review & editing: A.K.S., Yu.L.T., E.V.K.

Conflict of interest

The authors declare no conflict of interest.

Additional information

Author IDs:
Alexey Subanakov, Scopus ID 23101745800;
Yunna Tushinova, Scopus ID 6507295454;
Evgeny Kovtunets, Scopus ID 57216460806;
Tatyana Spiridonova, Scopus ID 57198791455;
Bair Bazarov, Scopus ID 7004745799.

Websites:
The Banzarov State University of Buryatia, https://www.binm.ru/en/;
The Banzarov State University of Buryatia, https://en.bsu.ru/.

References

1. Kharitonova EP, Voronkova VI, Belov DA, Orlova EI. Fluorite-like compounds with high anionic conductivity in Nd_2MoO_6 – Bi_2O_3 system. Int J Hydrogen Energy 2016;41:10053–9. doi: 10.1016/J.IJHYDENE.2016.03.046

2. Martínez-Lope MJ, Alonso JA, Sheptyakov D, Pomjakushin V. Preparation and structural study from neutron diffraction data of $Pr_5Mo_3O_{16}$. J Solid State Chem 2010;183:2974–8. doi:10.1016/J.JSSC.2010.10.015

3. Berezhnaya TS, Chebyshev KA. Fluorite-like phases in the La_2MoO_6 – Sm_2MoO_6 – MoO_3 system: Homogeneity region, crystal structure, and conductive properties. Ceram Int 2024;50:49803–13. doi:10.1016/j.ceramint.2024.09.323

4. Shlyakhtina A V., Lyskov N V., Šalkus T, Kežionis A, Patrakeev M V., Leonidov IA, et al. Conductivity and oxygen diffusion in bixbyites and fluorites $Ln_{6-x}MoO_{12-\delta}$ (Ln = Er, Tm; x = 0, 0.5). Int J Hydrogen Energy 2021;46:16965–76. doi:10.1016/j.ijhydene.2021.02.029

5. Voronkova VI, Leonidov IA, Kharitonova EP, Belov DA, Patrakeev M V., Leonidova ON, et al. Oxygen ion and electron conductivity in fluorite-like molybdates $Nd_5Mo_3O_{16}$ and Pr_5Mo_3O16. J Alloys Compd 2014;615:395–400. doi:10.1016/j.jallcom.2014.07.019

6. Schildhammer D, Fuhrmann G, Petschnig L, Kogler M, Penner S, Weinberger N, et al. Ion conductivity in cubically-stabilized fluorite-like structured $Er_5CeMoO_{12.5}$ and $Yb_5MMoO_{12.5}$ (M = Ce, Zr) solid solutions. Solid State Sci 2016;62:22–8. doi:10.1016/j.solidstatesciences.2016.10.011

7. Get'Man EI, Chebyshev KA, Pasechnik L V., Ardanova LI, Selikova NI, Radio S V. Isomorphous substitutions and conductivity in molybdates $Nd_{5-x}Ln_xMo_3O_{16+y}$ (y~0.5), where Ln = La, Ce, Pr. J Alloys Compd 2016;686:90–4. doi:10.1016/j.jallcom.2016.06.005

8. Shlyakhtina A V., Lyskov N V., Kolbanev I V., Shchegolikhin AN, Karyagina OK, Shcherbakova LG. Key trends in the proton conductivity of $Ln_{6-x}MoO_{12-\delta}$ (Ln = La, Nd, Sm, Gd -Yb; x = 0, 0.5, 0.6, 0.7, 1) rare-earth molybdates. Int J Hydrogen Energy 2021;46:16989–98. doi:10.1016/j.ijhydene.2021.01.129

9. Tolstov KS, Politov B V., Zhukov VP, Chulkov E V., Kozhevnikov VL. Oxygen non-stoichiometry and phase

decomposition of double perovskite-like molybdates $Sr_2MMoO_{6-\delta}$, where M = Mn, Co, and Ni. Mater Lett 2022;316:132039. doi:10.1016/j.matlet.2022.132039

10. Rajendran DN, Ravindran Nair K, Prabhakar Rao P, Sibi KS, Koshy P, Vaidyan VK. Ionic conductivity in new perovskite type oxides: $NaAZrMO_6$ (A = Ca or Sr; M = Nb or Ta). Mater Chem Phys 2008;109:189–93. doi:10.1016/j.matchemphys.2007.11.033

11. Panda D, Hota SS, Choudhary RNP. Development of a novel triple perovskite barium bismuth molybdate material for thermistor-based applications. Mater Sci Eng B 2023;296:116616. doi:10.1016/j.mseb.2023.116616

12. Belyakov SA, Shkerin SN, Kellerman DG, Plekhanov MS. The effect of Mo concentration on the electrical properties of $CaV_{1-x}Mo_xO_{3-\delta}$ (x=0.2 ÷ 0.6) anode materials for solid oxide fuel cells. Mater Res Bull 2020;129:1–7. doi:10.1016/j.materresbull.2020.110904

13. Filonova EA, Dmitriev AS, Pikalov PS, Medvedev DA, Pikalova EY. The structural and electrical properties of $Sr_2Ni_{0.75}Mg_{0.25}MoO_6$ and its compatibility with solid state electrolytes. Solid State Ionics 2014;262:365–9. doi:10.1016/j.ssi.2013.11.036

14. Tolstov KY, Politov B V., Zhukov VP, Chulkov E V., Kozhevnikov VL. The impact of atomic defects on high-temperature stability and electron transport properties in $Sr_2Mg_{1-x}Ni_xMoO_{6-\delta}$ solid solutions. J Alloys Compd 2021;883:160821. doi:10.1016/j.jallcom.2021.160821

15. Goutenoire F, Isnard O, Retoux R, Lacorre P. Crystal Structure of $La_2Mo_2O_9$, a New Fast Oxide–Ion Conductor. Chem Mater 2000;12:2575–80. doi:10.1021/CM991199L

16. Liu X, Fan H, Shi J, Dong G, Li Q. High oxide ion conducting solid electrolytes of bismuth and niobium co-substituted $La_2Mo_2O_9$. Int J Hydrogen Energy 2014;39:17819–27. doi:10.1016/j.ijhydene.2014.08.110

17. Marozau IP, Marrero-López D, Shaula AL, Kharton V V., Tsipis E V., Núñez P, et al. Ionic and electronic transport in stabilized β-$La_2Mo_2O_9$ electrolytes. Electrochim Acta 2004;49:3517–24. doi:10.1016/j.electacta.2004.03.022

18. Yang J, Wen Z, Gu Z, Yan D. Ionic conductivity and microstructure of solid electrolyte $La_2Mo_2O_9$ prepared by spark-plasma sintering. J Eur Ceram Soc 2005;25:3315–21. doi:10.1016/j.jeurceramsoc.2004.08.023

19. Savvin SN, Shlyakhtina A V., Borunova AB, Shcherbakova LG, Ruiz-Morales JC, Núñez P. Crystal structure and proton conductivity of some Zr-doped rare-earth molybdates. Solid State Ionics 2015;271:91–7. doi:10.1016/j.ssi.2014.12.003

20. Buzlukov AL, Baklanova Y V, Arapova IY, Savina AA, Morozov VA, Bardet M, et al. $Na_9In(MoO_4)_6$: synthesis, crystal structure, and Na^+ ion diffusion. Ionics (Kiel) 2021;27:4281–93. doi:10.1007/s11581-021-04226-3

21. Kaimieva OS, Mikhailovskaya ZA, Buyanova ES, Petrova SA, Pankrushina EA. Structure and Electrical Conductivity of Bismuth- and Germanium-Doped Calcium Molybdates. Russ J Inorg Chem 2023;68:386–95. doi:10.1134/S0036023623600235

22. Sonni M, Zid MF, Hlil EK, Zaidat K, Rossignol C, Obbade S. Na/Li substitution effect on the structural, electrical and magnetic properties of $LiCr(MoO_4)_2$ and β–$Li_{0.87}Na_{0.13}Cr(MoO_4)_2$. J Alloys Compd 2021;854:154740. doi:10.1016/j.jallcom.2020.154740

23. Gillie LJ, de Souza SA, Sheptyakov D, Reeves-McLaren N, Pasero D, West AR. Synthesis, structural characterization and Li^+ ion conductivity of a new vanado-molybdate phase, $LiMg_3VMo_2O_{12}$. J Solid State Chem 2010;183:2589–97. doi:10.1016/j.jssc.2010.08.042

24. Kotova IY, Savina AA, Vandysheva AI, Belov DA, Stefanovich SY. Synthesis, crystal structure and electrophysical properties of triple molybdates containing silver, gallium and divalent metals. Chim Techno Acta 2018;5:132–43. doi:10.15826/chimtech.2018.5.3.02

25. Savina AA, Solodovnikov SF, Basovich OM, Solodovnikova ZA, Belov DA, Pokholok K V., et al. New double molybdate $Na_9Fe(MoO_4)_6$: Synthesis, structure, properties. J Solid State Chem 2013;205:149–53. doi:10.1016/j.jssc.2013.07.007

26. Liu H, Zhu Y, Zhu J, Wang W, Zhang Z. Negative thermal expansion performance of $(NaMg)_xCr_{2-x}(MoO_4)_3$ (0≤x≤1) ceramics. Ceram Int 2024;50:39122–8. doi:10.1016/j.ceramint.2024.07.278

27. Zhang H, Nawaz A, Huang F, Zhang Z, Hongfei Liu. Synthesis, negative thermal expansion and optical performances of $In_{0.5}Sc_{1.5}Mo_3O_{12}$ thin films via sol-gel spin coating. Ceram Int 2024;50:25541–7. doi:10.1016/j.ceramint.2024.04.288

28. Liu H, Zhang H, Huang F, Zhu J, Wang W, Zeng X, et al. Preparation of $In_{0.5}Sc_{1.5}Mo_3O_{12}$ nanofibers and its negative thermal expansion property. Ceram Int 2023;49:31627–33. doi:10.1016/j.ceramint.2023.07.116

29. Nasri R, Larbi T, Amlouk M, Faouzi Zid M. Enhanced photocatalytic removal of azo dye by the $K_3NaCo_4(MoO_4)_6/H_2O_2$ system. Inorg Chem Commun 2024;165:112556. doi:10.1016/j.inoche.2024.112556

30. Swathi S, Yuvakkumar R, Senthil Kumar P, Ravi G, Thambidurai M, Dang C, et al. PEG mediated tetragonal calcium molybdate nanostructures for electrochemical energy conversion applications. Int J Hydrogen Energy 2022;47:26013–22. doi:10.1016/j.ijhydene.2022.03.023

31. Gao W, Sha R, Ai J. Synthesis and Properties of a Red $Na_5Zn_2Gd_{1-x}(MoO_4)_6:xEu^{3+}$ Phosphor. Crystals 2024;14. doi:10.3390/cryst14110933

32. Klevtsova R.F., Bazarova Zh.G., Klevtsov P.V., Alekseev V.I., Arkhincheeva S.I., Glinskaya L.A. BBG. Crystal structure study of $K(Mg_{0.5}Zr_{0.5})(MoO_4)_2$ ternary molybdate. Zhurnal Strukt Khimii 1995;36:891–4.

33. Klevtsova RF, Bazarov BG, Glinskaya LA, Bazarova TT, Fedorov KN, Victorvich K, et al. Thallium magnum zirconium molybdate $Tl_5Mg_{0.5}Zr_{1.5}(MoO_4)_6$: Synthesis, crystal structure, and properties. Russ J Inorg Chem 2003;48:1410–3.

34. Tushinova YL, Bazarov BG, Kovtunets E V, Bazarova JG. Phase formation in the $Ag_2MoO_4–Rb_2MoO_4–Hf(MoO_4)_2$ system. Kondens Sredy i Mezhfaznye Granitsy = Condens Matter Interphases 2021;23:594–9. doi:10.17308/KCMF.2021.23/3679

35. Coelho AA. Topas: General Profile and Structure Analysis Software for Powder Diffraction Data. Bruker AXS, 2005.

36. Dinnebier RE, Leineweber A, Evans JSO. Rietveld refinement practical powder diffraction pattern analysis using TOPAS. 2019. doi:10.1515/9783110461381-201

37. Bubnova RS, Firsova VA, Filatov SK. Software for determining the thermal expansion tensor and the graphic representation of its characteristic surface (theta to tensor-TTT). Glas Phys Chem 2013;39:347–50. doi:10.1134/S108765961303005X

38. Chen H, Wong LL, Adams S. SoftBV – a software tool for screening the materials genome of inorganic fast ion conductors. Acta Crystallogr Sect B Struct Sci Cryst Eng Mater 2019;75:18–33. doi:10.1107/S2052520618015718

39. Aksenov SM, Pavlova ET, Popova NN, Tsyrenova GD, Lazoryak BI. Stoichiometry and topological features of triple molybdates $A_xB_yC_z(MoO_4)_n$ with the heteropolyhedral open MT-frameworks: Synthesis, crystal structure of Rb5{Hf1.5Co0.5(MoO4)6}, and comparative crystal chemistry. Solid State Sci 2024;151:107525. doi:10.1016/j.solidstatesciences.2024.107525

40. Grossman VG, Bazarova JG, Molokeev MS, Bazarov BG. New triple molybdate $K_5ScHf(MoO_4)_6$: Synthesis, properties, structure and phase equilibria in the $M_2MoO_4–Sc_2(MoO_4)_3–Hf(MoO_4)_2$ (M = Li, K) systems. J Solid State Chem 2020;283:4–9. doi:10.1016/j.jssc.2019.121143

41. Pet'Kov VI, Shipilov AS, Sukhanov M V. Thermal expansion of $MZr_2(AsO_4)_3$ and $MZr_2(TO_4)_x(PO_4)_{3-x}$ (M = Li, Na, K, Rb, Cs; T = As, V). Inorg Mater 2015;51:1079–85. doi:10.1134/S002016851510012X

42. Kovtunets E, Tushinova Y, Logvinova A, Bazarova T, Bazarov B. Thermal expansion of ternary molybdate $K_5[Mn_{0.5}Zr_{1.5}](MoO_4)_6$. ESSUTM Bull 2024;94:90–7. doi:10.53980/24131997_2024_3_90

43. Kovtunets E, Spiridonova T, Tushinova Y, Logvinova A, Bazarova T, Bazarov B. Thermal expansion and ionic conductivity of $K_5Pb_{0.5}Zr_{1.5}(MoO_4)_6$. Izv Vuzov Prikl Khimiya i Biotekhnologiya 2024;14:106–11. doi:10.21285/achb.939

44. Petrushina MY, Korenev S V., Dedova ES, Gubanov AI. MATERIALS AM_2O_8 (A = Zr, Hf; M = W, Mo) WITH NEGATIVE THERMAL EXPANSION. J Struct Chem 2020;61:1655–80. doi:10.1134/S0022476620110013

45. Dorzhieva SG, Bazarova JG, Bazarov BG. Exploration of Phase Equilibria in the Triple Molybdate System, Electrical Properties of New $Rb_5M_{1/3}Zr_{5/3}(MoO_4)_6$ (M-Ag, Na) Phases. J Phase Equilibria Diffus 2021;42:824–30. doi:10.1007/S11669-021-00927-4/FIGURES/7

46. Spiridonova TS, Solodovnikov SF, Molokeev MS, Solodovnikova ZA, Savina AA, Kadyrova YM, et al. Synthesis, crystal structures, and properties of new acentric glaserite-related compounds $Rb_7Ag_{5-3x}Sc_{2+x}(XO_4)_9$ (X = Mo, W). J Solid State Chem 2022;305:122638. doi:10.1016/j.jssc.2021.122638

47. Spiridonova TS, Solodovnikov SF, Savina AA, Kadyrova YM, Solodovnikova ZA, Yudin VN, et al. New triple molybdate $Rb_2AgIn(MoO_4)_3$: synthesis, framework crystal structure and ion-transport behaviour. Acta Crystallogr Sect C Struct Chem 2018;74:1603–9. doi:10.1107/S2053229618014717